PHYSICAL REVIEW APPLIED **1,** 014002 (2014)

Three-Dimensional Holographic Refractive-Index Measurement of Continuously Flowing Cells in a Microfluidic Channel

Yongjin Sung,[1,*] Niyom Lue,[1] Bashar Hamza,[2] Joseph Martel,[2] Daniel Irimia,[2]
Ramachandra R. Dasari,[1] Wonshik Choi,[3] Zahid Yaqoob,[1] and Peter So[1,4]
[1]*Laser Biomedical Research Center, Massachusetts Institute of Technology,*
Cambridge, Massachusetts 02139, USA
[2]*BioMEMS Resource Center, Massachusetts General Hospital, and Harvard Medical School,*
Charlestown, Massachusetts 02129, USA
[3]*Department of Physics, Korea University, Seoul 136-701, Korea*
[4]*Department of Mechanical Engineering and Department of Biological Engineering,*
Massachusetts Institute of Technology, Cambridge, Massachusetts 02139, USA
(Received 12 December 2013; published 27 February 2014)

The refractive index of biological specimens is a source of intrinsic contrast that can be explored without any concerns of photobleaching or harmful effects caused by extra contrast agents. In addition, the refractive index contains rich information related to the metabolism of cells at the cellular and subcellular levels. Here, we report a no-moving-parts approach that provides three-dimensional refractive-index maps of biological samples continuously flowing in a microfluidic channel. Specifically, we use line illumination and off-axis digital holography to record the angular spectra of light scattered from flowing samples at high speed. Applying the scalar diffraction theory, we obtain accurate refractive-index maps of the samples from the measured spectra. Using this method, we demonstrate label-free three-dimensional imaging of live RKO human colon cancer cells and RPMI8226 multiple myeloma cells, and obtain the volume, dry mass, and density of these cells from the measured three-dimensional refractive-index maps. Our results show that the reported method, alone or in combination with the existing flow cytometry techniques, shows promise as a quantitative tool for stain-free characterization of a large number of cells.

DOI: 10.1103/PhysRevApplied.1.014002

I. INTRODUCTION

Refractive index serves as a source of intrinsic contrast in a variety of imaging modalities including optical coherence tomography [1,2] and light-scattering spectroscopy [3,4]. At the same time, the refractive index can be related to the density of organic molecules [5–7], and its volume integral can provide the total amount of nonaqueous content in a cell [8–10] or organelles [11]. Variance and change in the refractive index of cells are also linked to carcinogenic transformations [12,13]. The refractive index of homogeneous bulk materials can be obtained with a critical-angle refractometer measuring the critical angle of a specimen with respect to the other material with known refractive index [14]. For thin-layered materials, ellipsometry measuring depolarization of the incident light is known to be accurate [14]. Measuring the refractive index of a nonhomogeneous specimen such as biological cells requires a more delicate approach.

The refractive index can be related to the speed of light wave inside a material [15]. Therefore, wave-front distortion, which represents the total phase (time) delay of the light wave due to a specimen, can be connected to the three-dimensional (3D) refractive-index map of the specimen. The wave-front distortion can be measured with a Shack-Hartman wave-front sensor [16,17], interferometry [18–21], or inline holography (also called propagation-based methods) [22,23]. Among these techniques, interferometry is particularly appropriate in the optical regime, where the light sources with a reasonably large coherence length are readily available. The wave-front measurement for a single angle of illumination can provide only partial information of the 3D specimen; thus, one has to use a tomographic acquisition method in conjunction with the wave-front measurement. Typically, a collimated laser beam is used and its angle of incidence onto the sample is varied by rotating the sample or scanning the direction of illumination beam [24–27]. It has been also demonstrated that one can obtain the refractive-index map with a spatially incoherent beam and scanning the objective focus through the sample [28]. In either approach, however, the sample has to be stationary while the illumination direction or the objective focus is varied, which limits the throughput of imaging.

From the Huygens principle [15], a plane wave can be synthesized from parallel line-focused beams, whose relative phase determines the wave propagation direction, and vice versa. Thus, scanning a line-focused beam across a sample, we can collect the information equivalent to that

---

[*] To whom all correspondence should be addressed.
yongjin.sung@gmail.com

acquired with varying the illumination angle of a plane wave onto the sample. Importantly, in the former method we measure the angular spectra of scattered light, while in the latter method we directly measure distorted wave fronts after the sample. From the angular spectra acquired for varying locations of the line-focused beam, we can obtain the depth-resolved refractive-index map. This technique, called wave synthesis or synthetic-aperture tomography, was demonstrated first in the ultrasound regime [29], and recently in the optical regime [30]. In our previous demonstration [30], the angular spectra, which are complex quantities, were measured with phase shifting interferometry (PSI). In PSI, the sample has to be stationary during the phase-shifting step; thus, the images are acquired in a discrete fashion, which cannot be applied to continuously flowing samples. For tomographic reconstruction, we adopted a filtered back-projection algorithm [31], which is not ideal for thick cells. In this study, we overcome these limitations by adopting off-axis digital holography for the angular spectra measurement and applying an algorithm based on the scalar diffraction theory for the tomographic reconstruction. Using a microfluidic channel designed for our high-numerical-aperture setup, we demonstrate, for the first time within our knowledge, 3D refractive-index imaging of cells continuously flowing in a microfluidic channel.

II. METHODS

Consider that we illuminate a specimen with the light whose complex amplitude can be represented by u_{in}. From the scalar diffraction theory, the complex amplitude of scattered light can be written as [32]

$$u_{\mathrm{scat}}(\vec{r}) = \int u_{\mathrm{in}}(\vec{r}')V(\vec{r}')G(|\vec{r}-\vec{r}'|)d^3r', \tag{1}$$

where $G(r) = \exp(ikr)/4\pi r$ is the Green's function for the Helmholtz equation. λ is the wavelength of the incident light in the medium, and $k = 2\pi/\lambda$ is the wave number. The function $V(x,y,z) = k^2\{1-[n(x,y,z)/n_0]^2\}$ is the scattering potential of the specimen, in which $n(x,y,z)$ and n_0 represent the refractive indices of the specimen and surrounding medium, respectively. We note that for plane-wave illumination, Eq. (1) is reduced to the complex scattered field in conventional optical diffraction tomography [33]. In this study, we illuminate the specimen with a line-focused beam, which consists of multiple plane waves [34], and measure the angular spectra of the scattered light (see Fig. 1). For tomographic reconstruction, we record a series of the angular spectra $E_{\mathrm{samp}}(k_x,y;\eta)$ for varying locations η of the sample while it passes across the line-focused beam. The variable k_x is the spatial frequency coordinate corresponding to the spatial coordinate x. To remove any background phase due to optical aberration, we also record an angular spectrum $E_{\mathrm{bg}}(k_x,y)$ before starting the experiment. With the first-order Rytov approximation [29,35], the measured angular spectra $E_{\mathrm{samp}}(k_x,y;\eta)$ and $E_{\mathrm{bg}}(k_x,y)$ can be related to the specimen's scattering potential $V(x,y,z)$ as

$$\bar{u}_{\mathrm{scat}}(k_x,y;\eta) = [i4\pi w(k_x)]^{-1}\int \tilde{V}[k_x-p,y,w(k_x)-w(p)]\exp[i2\pi(k_x-p)\eta]dp. \tag{2}$$

Here, $\bar{u}_{\mathrm{scat}}(k_x,y;\eta) = \log[E_{\mathrm{samp}}(k_x,y;\eta)/E_{\mathrm{bg}}(k_x,y)]$, and $w(u) = (k^2-u^2)^{1/2}$. Taking the Fourier transform of Eq. (2) with respect to y and η, we obtain Eq. (3), which simply relates the measured angular spectra with the specimen's scattering potential in the spatial frequency space.

$$\tilde{V}(k_x,k_y,k_z) = i4\pi w(k_x)\tilde{\bar{u}}_{\mathrm{scat}}(k_x,k_y;k_\eta), \tag{3}$$

where $k_z = w(k_x) - w(k_x - k_\eta)$. $\tilde{\bar{u}}_{\mathrm{scat}}(k_x,k_y;k_\eta)$ is the two-dimensional Fourier transform of $\bar{u}_{\mathrm{scat}}(k_x,y;\eta)$ with respect to y and η.

Figure 2 shows a schematic of the experimental setup used for this study. It is based on Mach-Zehnder interferometry, and adopts a He-Ne laser ($\lambda = 633$ nm) as the light source. We generate a line-focused beam with a high-NA condenser lens (Olympus, numerical aperture = 1.4) and a cylindrical lens ($f = 100$ mm, where f is the focal length of the lens). We flow samples across this line-focused beam in a microfluidic channel, and collect the angular spectra of scattered light with a high-NA objective lens. The beam after the tube lens is expanded using a cylindrical lens CL 2 ($f = 400$ mm). Two other cylindrical lenses CL 1 ($f = 200$ mm) and CL 3 ($f = 200$ mm) are installed in the beam path to deliver the image in a 4-f configuration along the nonfocusing axis. A complementary metal-oxide semiconductor (CMOS) camera (1024PCI, Photron, Inc.) located at the back focal plane of CL 2 records the complex angular spectra while the samples flow across the line-focused beam. Importantly, we adopt off-axis holography and record both the amplitude and phase of angular spectrum in a single shot for each location of the flowing sample. Specifically, we tilt the reference beam slightly with respect to the sample beam for the raw interferogram images to have about a three-pixel fringe period [19]. The camera is triggered by an internal clock to capture the interferograms at the frame rate of 5000 frames/ sec. Both the high frame rate for the camera and the high NA for

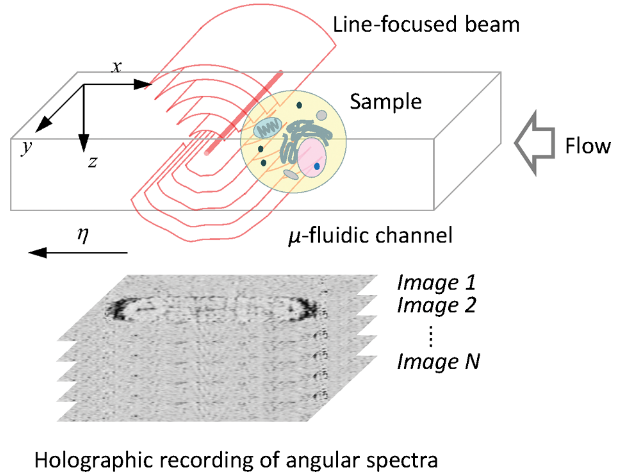

FIG. 1 (color online). Schematic of three-dimensional holographic imaging of continuously flowing cells.

capturing high-angle scattering are important to achieving high spatial resolution in our method. In this study, we adjust the flow speed so as to acquire about 500 images per cell. The corresponding speed of cells in the channel is about 150 μm/ sec assuming the cell diameter of 15 μm. The thickness of the upper polydimethylsiloxane (PDMS) layer of microfluidic device has to be smaller than the working distance of the high-NA condenser lens (~200 μm). In addition, to minimize the cell tumbling and rotation within the channel, we design the channel height to be slightly larger than the maximum diameter of cells. Using precise control of the soft-lithography process (see Sec. VI for more explanation), we make a microfluidic device that meets these criteria. The dimension of the channel cross section used for this study is 30×400 μm^2 (height × width).

III. RESULTS

Figure 3 shows the data processing for raw interferogram images. Figure 3(a) shows an example interferogram image recorded using our setup (Fig. 2), and Fig. 3(b) is the amplitude of the Fourier transform of Fig. 3(a). The region in the dotted circle contains the information about the specimen, which is separated from the unscattered light (the peak at the center). Selecting the dotted region, moving it to the center, and taking the inverse Fourier transform, we retrieve the complex angular spectra $E_{\mathrm{samp}}(k_x, y; \eta)$ for each location η of the sample (see Sec. VI for a detailed description). Figures 3(c) and 3(d) show the amplitude and phase, respectively, of the angular spectra retrieved from Fig. 3(a). Similarly, we process the other raw interferogram images to obtain a series of angular spectra for varying locations of the flowing specimen [Fig. 4(a)]. Taking the Fourier transform of the data cube along the k_x and η axes, we can obtain a sinogram [Fig. 4(b)], where x and y are spatial coordinates and k_η corresponds to the angle of illumination. Instead, we take the Fourier transform of the original data cube with respect to y and η, and map it in the 3D spatial frequency space using the Fourier diffraction theorem, Eq. (3). Figure 4(c) shows cross-section images of the spatial frequency map $\tilde{V}$ of an RKO human colon cancer cell after the mapping. In our setup, we flow samples across a line-focused beam, which is equivalent to changing the angle of illumination along one axis in rotating-beam geometry [35]. Thus, the spatial resolution and optical sectioning capability are the same as those for plane-wave tomography adopting one-axis scanning, which explains an empty region resembling an apple core near the center of the image in Fig. 4(c)(i) [36]. The k_x-k_z cross section [Fig. 4(c)(ii)] shows a similarly empty region, which is due to the limited angular coverage of the condenser and objective lenses [37]. These empty regions

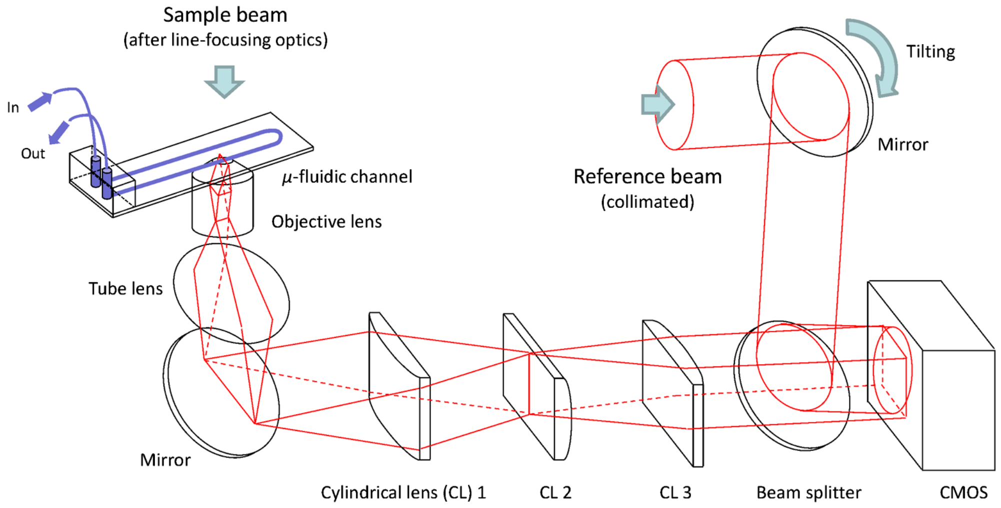

FIG. 2 (color online). Schematic of the experimental setup used in this study.

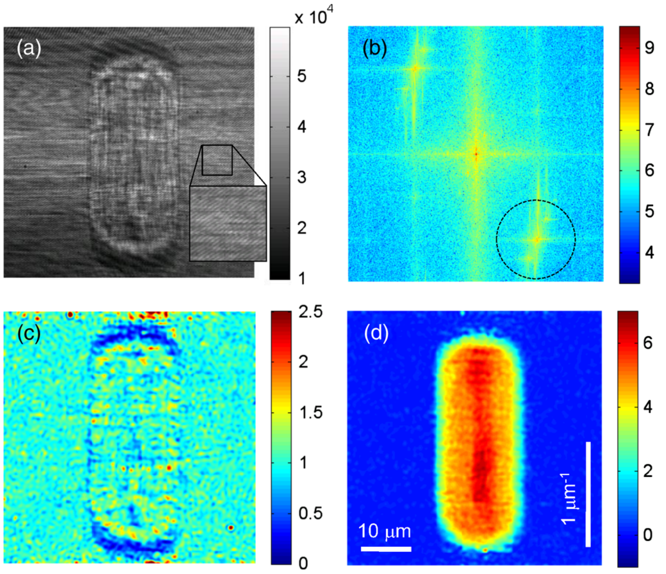

FIG. 3 (color online). Data processing to extract the amplitude and phase of angular spectrum. (a) An example of raw interferogram image. (b) Magnitude of the Fourier transform of (a), shown in a logarithmic scale (base 10). (c),(d) Amplitude and phase images, respectively, extracted from (b).

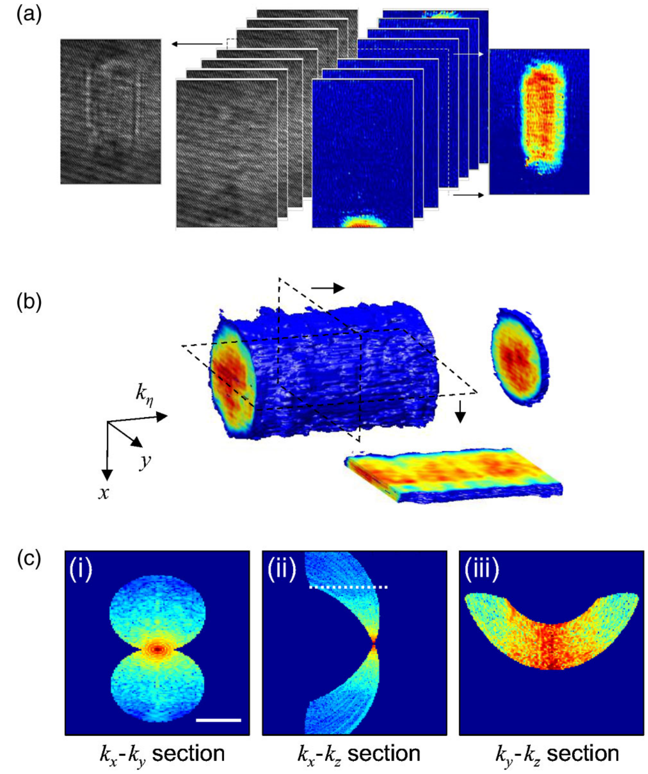

FIG. 4 (color online). Mapping of the complex fields in the spatial frequency space. (a) A series of raw interferogram images recorded for different locations of the sample and corresponding phase images. (b) Sinogram, phase images plotted for varying values of spatial frequency k_η. (c) Spatial frequency spectrum of an RKO human colon cancer cell after the mapping: (i) k_x-k_y cross section; (ii) k_x-k_z cross section; and (iii) k_y-k_z cross section containing the dotted line in (ii). Scale bar (1 μm^{-1}) in (i) also applies to (ii) and (iii).

in the 3D spatial frequency map generate missing angle artifacts, elongation of the object in the reconstructed image, and underestimation of its refractive index. In this work, we adopt an algorithm utilizing the non-negativity of mass density, which accurately provides mean refractive-index values of cells [37]. For more complete compensation of the missing angle data, we can apply additional constraints, e.g., piecewise smoothness of the refractive-index profile, in the reconstruction process. Figure 5(a) shows the refractive-index map of an RKO human colon cancer cell after 200 iterations. In Fig. 5(a)(i), the center cross section of the 3D map clearly shows the nucleus and nucleolus of the cell. Figure 5(a)(ii) shows horizontal cross sections extracted for varying heights (1.5-μm spacing between the slices), which show varying structures in the cell with high optical sectioning capability.

Measuring the mass and volume of cells is connected to the fundamental question of biology: how the cells grow and their growth is regulated [10,38,39]. The refractive index of a biological specimen is known to be proportional to the concentration of organic molecules within the specimen [5–7]. Adopting this relationship, we can obtain the density of nonaqueous materials inside a cell, called dry density, from

$$\rho_{\text{dry}} = (1/\alpha)[n(x,y,z) - n_0], \qquad (4)$$

where the quantity α is the average specific refractive-index increment $\alpha = 0.190\ (\text{g/mL})^{-1}$ [40]. The volume of a sample is calculated by counting the number of voxels after applying thresholding to the reconstructed refractive-index map. The total dry mass within the cell can be obtained by taking the integral of the 3D density map, given by Eq. (4), over the cell volume. To validate our method, we image 10-μm polystyrene beads flowing in the index matching oil of refractive index 1.54. The diameter of polystyrene beads ($N = 8$) is measured to be (9.89 ± 0.35) μm, and the refractive index n is determined as 1.583 ± 0.005. These values match well with the values provided by the manufacturer (10 μm diameter, $n = 1.585$). When normalized with the manufacturer's specifications, the measured volume and refractive index of the beads are 0.980 ± 0.110 and 0.986 ± 0.032, respectively. These values may be used as estimates for the accuracy of the proposed method in volume and density measurement. Next, we image RKO human colon cancer cells and RPMI8226 human multiple myeloma cells ($N = 60$ each) [see Figs. 5(b)(i)–5(b)(iii)]. The distributions of mass and volume are broad because the measurement is applied to an asynchronous population of cells. Interestingly, the mean volume of RPMI8226 cells [(1654 ± 69) fl] is (11.6 ± 6.3)% smaller than that of RKO cells [(1845 ± 70) fl], while the mean dry mass of

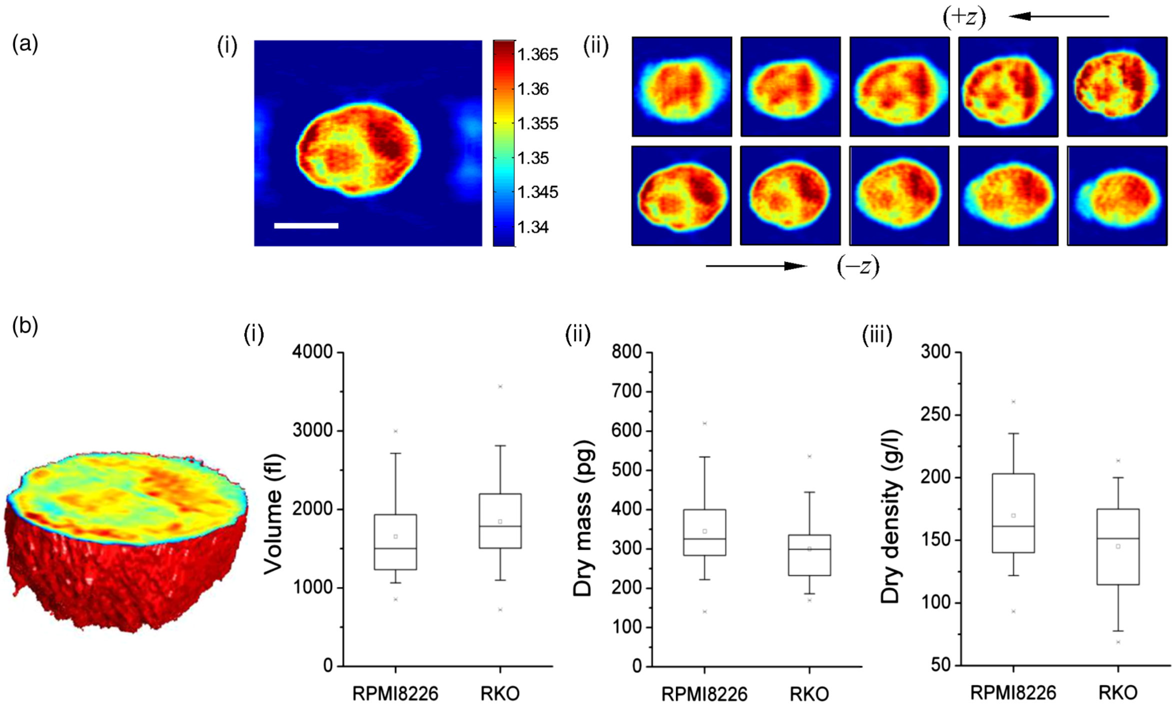

FIG. 5 (color online). (a) Reconstructed refractive-index map of an RKO cell: (i) center cross section (scale bar, 10 μm) and (ii) cross sections at multiple heights extracted with 1.5-μm interval. (b) Volume, dry mass, and dry density of RPMI8226 and RKO cells: (i) volume of RPMI8226 [(1654 ± 69) fl] and RKO cells [(1845 ± 70) fl]; (ii) dry mass of RPMI8226 [(345 ± 13) pg] and RKO cells [(300 ± 11) pg]; (iii) dry density of RPMI8226 [(170 ± 5) g/l] and RKO cells [(145 ± 5) g/l]. $N = 60$ for both cells in (i), (ii), and (iii). A volume-rendered image of the same cell in Fig. 5(a) is shown on the left with the center cross section exposed.

RPMI8226 cells [(345 ± 13) pg] is $(15.0 \pm 5.8)\%$ larger than that of RKO cells [(300 ± 11) pg]. We note that the volume of two cell types is not statistically different ($p > 0.05$, two-tailed t-test, $N = 60$), but RPMI8226 cells [(170 ± 5) g/l] have $(17.2 \pm 5.4)\%$ larger mean (dry) density than RKO cells [(145 ± 5) g/l] due to their larger mass. Both the dry mass and density are measured to be significantly different in two cell types ($p < 0.01$, two-tailed t-test, $N = 60$).

IV. DISCUSSION

A major contrast mechanism in flow cytometry is fluorescence, externally administered or generated through genetic manipulation. However, the fluorescent labeling is not always a viable option, especially for primary cells. In addition, accurate quantification of the target molecules is challenged by photobleaching and nonuniform binding of the labeling agents [41]. Three-dimensional refractive-index measurement enables one to quantify the cell metabolism by providing the mass of the entire cell and internal organelles with minimal perturbation [11]. Using plane-wave tomography, we showed that adherently growing cells have size-dependent growth rate as floating cells, while division asymmetry is higher in the former [10]. In conjunction with low-noise diffraction phase microscopy, we also showed that mammalian chondrocytes undergo three distinct phases of volume increase [42]. Recent results show that molecular-specific signatures of cells can be also obtained from refractive-index measurement at multiple wavelengths [11,43,44].

The refractive index of a complex biological specimen can be obtained with measuring the sample-induced wavefront distortion for varying illumination angles [24–26]. Inspired by synthetic aperture tomography in ultrasound imaging [29], we demonstrated a method to obtain the refractive index of cells translated across a line-focused laser beam [30]. In our previous demonstration, however, the angular spectra of light scattered from the sample were measured using phase-shifting interferometry, which required the sample to be stationary for each location of the sample. Thus, we mounted the sample on a translation stage and translated it across the line-focused beam in a discrete fashion, which cannot be applied to continuously flowing samples. We also adopted the inverse Radon transform for tomographic reconstruction, which generated the diffraction artifact when applied in the optical imaging [35].

In the present study, we demonstrate 3D refractive-index imaging of continuously flowing cells in a microfluidic channel. For this, we adopt off-axis digital holography that can measure the complex angular spectrum in a single shot for each location of the flowing sample. For tomographic reconstruction, we adopt an algorithm based on the scalar diffraction theory to correct the artifacts due to defocused organelles and cells flowing at different heights. Using these methods, we obtain 3D maps of refractive index of two cell types in the flow configuration, from which we quantify the volume, dry mass, and dry density of the cells. The existing method of obtaining the cell density in flow configuration relies on the buoyant mass measurement using a suspended microchannel resonator for two different density liquids [45]. Removing the liquid-switching step, the method proposed in this study can be applied for high throughput or long-term imaging of cells in an intact, natural condition. In addition, our method can provide the 3D density map inside the cells.

The tomographic reconstruction algorithm derived and adopted in this study assumes that cells' vertical position in the channel is fixed and their rotation is negligible for the period of data collection or for complete passage of each cell across the line-focused beam. Observing the cells under a collimated laser illumination and with a high-speed camera, we confirm that cell tumbling is minimal for the design and flow conditions used in this study. However, without a mechanism to stabilize the cells flowing in a microfluidic channel [46–48], the possibility of cell rotation cannot be completely ruled out. In microfluidic systems the cell rotation is caused by shear forces acting on a cell which is proportional to the speed of the flow and inversely with size of the cell. A cell larger than half the height of the channel is less affected by this shear as the difference in fluid velocity on the sides of the cell diminishes when the cell straddles the midheight of the channel. By imaging PDMS beads with air defects, we estimate that the maximum rotation of cells (mean diameter $\sim 15\ \mu$m) during the data acquisition (0.1 sec) is about 4° at the Reynolds number used in this study (5×10^{-3}). The minimal effect of this rotation is further confirmed by the sharp boundaries of the cell and nucleus in the reconstructed image of Fig. 5(a)(i) where the rotation would likely cause blurring.

V. CONCLUSION

We report a method that provides the 3D refractive-index maps of cells continuously flowing in a microfluidic channel. Specifically, we flow samples across a line-focused beam, and record the angular spectra of scattered light using off-axis digital holography. The microfluidic device is carefully designed and fabricated to minimize cell tumbling as well as to enable the use of high-NA condenser and objective lenses. For tomographic reconstruction of a 3D refractive-index map, we adopt an algorithm derived from the scalar diffraction theory to compensate for defocusing of the cells in the channel and to reduce the diffraction artifacts that arise from defocused organelles inside cells. An iterative constraint algorithm is applied to minimize the artifacts due to limited angular coverage of the incident beam. Importantly, the reported method does not require any moving elements, and permits high-speed acquisition of desired information. The proposed method therefore holds great promise for single-cell characterization; it can be readily incorporated into the downstream of existing flow cytometry configurations for additional cell screening based on accurate 3D refractive-index mapping. The measured refractive-index map can be further related to the distribution of mass at cellular or subcellular levels, and thus the metabolism of cellular organelles.

VI. MATERIALS AND METHODS

A. Sample preparation

RKO human colon cancer cells are cultured in Dulbecco Modified Eagle medium (Invitrogen, 21063-029) supplemented with 10% FBS (Invitrogen, 10438026) and 1% 100 × penicillin-streptomycin solution (Invitrogen, 15140-122). RPMI8226 human multiple myeloma cells are cultured in RPMI 1640 media (Invitrogen, 11835-030) supplemented with 10% FBS, and 1% 100 × penicillin-streptomycin solution. At 70%–80% confluency, cells are collected with 0.25% Trypsin-EDTA (Invitrogen, 25200-114), diluted 1∶100 in fresh culture media, and injected into the microfluidic channel with a syringe. 10-μm polystyrene beads and refractive-index liquids are purchased from Polysciences, Inc. (17136-5) and Cargille (1809X), respectively. Beads with air defects are created by vortexing a mixture of uncured PDMS (1∶10 ratio of curing agent and PDMS elastomer base that is thoroughly mixed) and water with 0.1% Tween 20 (Sigma-Aldrich, P9416) at an overall ratio of 10∶1 (water to PDMS). Once vortexed, the emulsion is then heated to 65°C in a water bath for 6 h to cure the PDMS particles. The bead solution is then filtered to obtain beads of a certain diameter and sedimentation can be used to collect particles with air defects.

B. Holographic recording of angular spectra

The amplitude and phase of angular spectra are recorded using off-axis holography. Figure 3 illustrates the process to analyze raw interferogram images. The irradiance [Fig. 3(a)] on the detector can be expressed as

$$I(x,y) = I_S(x,y) + I_R + 2\sqrt{I_S(x,y)I_R}\cos[2\pi(px+qy) - \Delta\varphi(x,y)], \tag{5}$$

where $I_S(x,y)$ and I_R are the irradiances of the sample and reference beams, respectively, and $\Delta\varphi(x,y)$ is the phase difference between the two beams. The vector (p,q) indicates the relative angle of incidence of the sample beam on the detector plane with respect to the reference beam. The magnitude and direction of the vector explain the spacing and orientation of the spatial fringes [see the inset of

Fig. 3(a)], respectively, in the raw interferogram. Figure 3(b) shows the magnitude of the Fourier transform of Fig. 3(a) on a logarithmic scale (base 10). The region inside the dotted circle can be described by

$$\hat{I}(u, v) = \hat{\Phi}(u - p, v - q), \tag{6}$$

where $\hat{\Phi}(u, v)$ is the Fourier transform of $\Phi(x, y) = \sqrt{I_S(x, y) I_R} \exp[-i\Delta\varphi(x, y)]$. Thus, one can obtain the function $\Phi(x, y)$ by selecting the region in the dotted circle, moving it to the origin of the frequency coordinates, and taking its inverse Fourier transform. The images in Figs. 3(c)–3(d) are the amplitude and phase images, respectively, obtained from Fig. 3(a).

C. Fabrication of a microfluidic device

Microfluidic devices are manufactured by replica molding of polydimethylsiloxane (PDMS, Dow Corning, Midland, MI) on a microfabricated master mold. The mold is fabricated using a standard photolithographic technique as briefly described below. A silicon wafer is baked in an oven set to 200 °C for 30 min, cleaned with oxygen plasma (March, Concord, CA), and then spin coated with SU-8 25 photoresist (SU8, Microchem, Newton, MA) at 1850 rpm to achieve a final thickness of approximately 30 μm and processed following the standard protocol as recommended by the manufacturer. A thin layer of PDMS is prepared, degassed in a vacuum chamber for 1 h, and then spun on the wafer at 600 rpm for 15 sec. After baking for 8 h at 65 °C, the thin PDMS layer covering the master along with thicker, cured, and previously cut PDMS pieces (length approximately 1 cm, width approximately 0.5 cm, height approximately 0.3 cm) is exposed to 20 sec of oxygen plasma and bonded on the inlet and outlet regions. Next, the mold is baked at 75 °C for 10 min, cut, slowly peeled off the master mold, and then punched with a 0.75 mm puncher to define the inlet and the outlet holes of the device. Finally, a 48 × 65 mm No. 1 gold-coated cover glass (Fisher Scientific, Pittsburgh, PA) along with the punched membrane-based channel device are exposed to 20 sec of oxygen plasma and carefully bonded at 75 °C for 10 min to define the microfluidic channels. Two pieces of flexible plastic tubing (Tygon, ID 0.010 inch × OD 0.030 inch, Greene Rubber Co., Woburn, MA) are cut to a length of ~3 cm and then inserted into the inlet and outlet holes of the device. A 30 g blunt needle (Brico Medical Supplies, Dayton, NJ) is then inserted into one of the tubes to allow for a syringe to be connected for sample loading purposes.

ACKNOWLEDGMENTS

This work is funded by the National Institutes of Health (9P41EB015871-26A1 and P41 EB002503) and Hamamatsu Photonics, Japan.

[1] D. Huang, E. A. Swanson, C. P. Lin, J. S. Schuman, W. G. Stinson, W. Chang, M. R. Hee, T. Flotte, K. Gregory, C. A. Puliafito, *et al.*, Optical coherence tomography, Science **254**, 1178 (1991).

[2] J. G. Fujimoto, Optical coherence tomography for ultrahigh resolution *in vivo* imaging, Nat. Biotechnol. **21**, 1361 (2003).

[3] V. Backman *et al.*, Detection of preinvasive cancer cells, Nature (London) **406**, 35 (2000).

[4] K. J. Chalut, J. H. Ostrander, M. G. Giacomelli, and A. Wax, Light scattering measurements of subcellular structure provide noninvasive early detection of chemotherapy-induced apoptosis, Cancer Res. **69**, 1199 (2009).

[5] R. Barer, Interference microscopy and mass determination, Nature (London) **169**, 366 (1952).

[6] R. Barer and S. Tkaczyk, Refractive index of concentrated protein solutions, Nature (London) **173**, 821 (1954).

[7] R. Barer, Refractometry and interferometry of living cells, J. Opt. Soc. Am. **47**, 545 (1957).

[8] M. Mir, Z. Wang, Z. Shen, M. Bednarz, R. Bashir, I. Golding, S. G. Prasanth, and G. Popescu, Optical measurement of cycle-dependent cell growth, Proc. Natl. Acad. Sci. U.S.A. **108**, 13124 (2011).

[9] G. Popescu, Y. K. Park, N. Lue, C. Best-Popescu, L. Deflores, R. R. Dasari, M. S. Feld, and K. Badizadegan, Optical imaging of cell mass and growth dynamics, Am. J. Physiol. Cell Physiol. **295**, C538 (2008).

[10] Y. Sung, A. Tzur, S. Oh, W. Choi, V. Li, R. R. Dasari, Z. Yaqoob, and M. W. Kirschner, Size homeostasis in adherent cells studied by synthetic phase microscopy, Proc. Natl. Acad. Sci. U.S.A. **110**, 16687 (2013).

[11] Y. Sung, W. Choi, N. Lue, R. R. Dasari, and Z. Yaqoob, Stain-Free quantification of chromosomes in live cells using regularized tomographic phase microscopy, PLoS One **7**, e49502 (2012).

[12] A. M. Zysk, E. J. Chaney, and S. A. Boppart, Refractive index of carcinogen-induced rat mammary tumours, Phys. Med. Biol. **51**, 2165 (2006).

[13] A. Wax, C. Yang, M. G. Müller, R. Nines, C. W. Boone, V. E. Steele, G. D. Stoner, R. R. Dasari, and M. S. Feld, *In situ* detection of neoplastic transformation and chemopreventive effects in rat esophagus epithelium using angle-resolved low-coherence interferometry, Cancer Res. **63**, 3556 (2003).

[14] S. Singh, Refractive index measurement and its applications, Phys. Scr. **65**, 167 (2002).

[15] B. E. Saleh, M. C. Teich, and B. E. Saleh, *Fundamentals of Photonics* (Wiley, New York, 1991), Vol. 22.

[16] B. Grimm, S. Goelz, and J. F. Bille, Objective measurement of wave aberrations of the human eye with the use of a Hartmann-Shack wave-front sensor, J. Opt. Soc. Am. A **11**, 1949 (1994).

[17] P. Bon, G. Maucort, B. Wattellier, and S. Monneret, Quadriwave lateral shearing interferometry for quantitative phase microscopy of living cells, Opt. Express **17**, 13080 (2009).

[18] K. Creath, Phase-measurement interferometry techniques, Prog. Opt. **26**, 349 (1988).

[19] T. Ikeda, G. Popescu, R. R. Dasari, and M. S. Feld, Hilbert phase microscopy for investigating fast dynamics in transparent systems, Opt. Lett. **30**, 1165 (2005).

[20] H. Iwai, C. Fang-Yen, G. Popescu, A. Wax, K. Badizadegan, R. R. Dasari, and M. S. Feld, Quantitative phase imaging using actively stabilized phase-shifting low-coherence interferometry, Opt. Lett. **29**, 2399 (2004).

[21] Z. Wang, L. Millet, M. Mir, H. Ding, S. Unarunotai, J. Rogers, M. U. Gillette, and G. Popescu, Spatial light interference microscopy (SLIM), Opt. Express **19**, 1016 (2011).

[22] M. Reed Teague, Deterministic phase retrieval: A Green's function solution, J. Opt. Soc. Am. **73**, 1434 (1983).

[23] N. Streibl, Phase imaging by the transport equation of intensity, Opt. Commun. **49**, 6 (1984).

[24] V. Lauer, New approach to optical diffraction tomography yielding a vector equation of diffraction tomography and a novel tomographic microscope, J. Microsc. **205**, 165 (2002).

[25] F. Charrière, A. Marian, F. Montfort, J. Kuehn, T. Colomb, E. Cuche, P. Marquet, and C. Depeursinge, Cell refractive index tomography by digital holographic microscopy, Opt. Lett. **31**, 178 (2006).

[26] W. Choi, C. Fang-Yen, K. Badizadegan, S. Oh, N. Lue, R. Dasari, and M. Feld, Tomographic phase microscopy, Nat. Methods **4**, 717 (2007).

[27] S. O. Isikman, W. Bishara, S. Mavandadi, F. W. Yu, S. Feng, R. Lau, and A. Ozcan, Lens-free optical tomographic microscope with a large imaging volume on a chip, Proc. Natl. Acad. Sci. U.S.A. **108**, 7296 (2011).

[28] P. Bon, S. Aknoun, J. Savatier, B. Wattellier, and S. Monneret, Tomographic incoherent phase imaging, a diffraction tomography alternative for any white-light microscope, Proc. SPIE Int. Soc. Opt. Eng. **8589**, 858918 (2013).

[29] D. Nahamoo, S. Pan, and A. C. Kak, Synthetic aperture diffraction tomography and its interpolation-free computer implementation, IEEE Trans. Sonics Ultrason. **31**, 218 (1984).

[30] N. Lue, W. Choi, G. Popescu, K. Badizadegan, R. R. Dasari, and M. S. Feld, Synthetic aperture tomographic phase microscopy for 3D imaging of live cells in translational motion, Opt. Express **16**, 16240 (2008).

[31] A. Kak and M. Slaney, *Principles of Computerized Tomographic Imaging* (Society for Industrial and Applied Mathematics, Philadelphia, 1988).

[32] M. Born and E. Wolf, *Principles of Optics: Electromagnetic Theory of Propagation, Interference and Diffraction of Light* (CUP Archive, New York, 1999).

[33] E. Wolf, Three-dimensional structure determination of semi-transparent objects from holographic data, Opt. Commun. **1**, 153 (1969).

[34] J. Goodman, *Introduction to Fourier Optics* (Roberts & Company Publishers, Englewood, 2005).

[35] Y. Sung, W. Choi, C. Fang-Yen, K. Badizadegan, R. Dasari, and M. Feld, Optical diffraction tomography for high resolution live cell imaging, Opt. Express **17**, 266 (2009).

[36] O. Haeberlé, K. Belkebir, H. Giovaninni, and A. Sentenac, Tomographic diffractive microscopy: Basics, techniques and perspectives, J. Mod. Opt. **57**, 686 (2010).

[37] Y. Sung and R. R. Dasari, Deterministic regularization of three-dimensional optical diffraction tomography, J. Opt. Soc. Am. A **28**, 1562 (2011).

[38] A. Tzur, R. Kafri, V. S. LeBleu, G. Lahav, and M. W. Kirschner, Cell growth and size homeostasis in proliferating animal cells, Science **325**, 167 (2009).

[39] S. Son, A. Tzur, Y. Weng, P. Jorgensen, J. Kim, M. W. Kirschner, and S. R. Manalis, Direct observation of mammalian cell growth and size regulation, Nat. Methods **9**, 910 (2012).

[40] H. Zhao, P. H. Brown, and P. Schuck, On the distribution of protein refractive index increments, Biophys. J. **100**, 2309 (2011).

[41] J. R. Lakowicz and B. R. Masters, Principles of fluorescence spectroscopy, J. Biomed. Opt. **13**, 029901 (2008).

[42] K. Cooper, S. Oh, Y. Sung, R. R. Dasari, M. W. Kirschner, and C. J. Tabin, Multiple phases of chondrocyte enlargement underlie differences in skeletal proportions, Nature (London) **495**, 375 (2013).

[43] M. T. Rinehart, N. T. Shaked, N. J. Jenness, R. L. Clark, and A. Wax, Simultaneous two-wavelength transmission quantitative phase microscopy with a color camera, Opt. Lett. **35**, 2612 (2010).

[44] D. Fu, W. Choi, Y. Sung, Z. Yaqoob, R. R. Dasari, and M. Feld, Quantitative dispersion microscopy, Biomed. Opt. Express **1**, 347 (2010).

[45] W. H. Grover, A. K. Bryan, M. Diez-Silva, S. Suresh, J. M. Higgins, and S. R. Manalis, Measuring single-cell density, Proc. Natl. Acad. Sci. U.S.A. **108**, 10992 (2011).

[46] C. B. Fuh, Split-flow thin fractionation, Anal. Chem. **72**, 266A (2000).

[47] J. C. Giddings, Optimization of transport-driven continuous SPLITT fractionation, Sep. Sci. Technol. **27**, 1489 (1992).

[48] P. R. Gascoyne and J. Vykoukal, Particle separation by dielectrophoresis, Electrophoresis **23**, 1973 (2002).